1-10-2009

Hubble Space Telescope Observations Of The Quasar PKS 0637-752: Equipartition Electron-Proton Jet From The Most Complete Spectral Coverage To Date

Kushal T. Mehta

Markos Georganopoulos

Eric S. Perlman

Charles A. Padgett

George Chartas

The Astrophysical Journal, 690:1706–1714, 2009 January 10 doi:10.1088/0004-637X/690/2/1706

HUBBLE SPACE TELESCOPE OBSERVATIONS OF THE QUASAR PKS 0637-752: EQUIPARTITION ELECTRON–PROTON JET FROM THE MOST COMPLETE SPECTRAL COVERAGE TO DATE

Kushal T. Mehta[1], Markos Georganopoulos[1,2], Eric S. Perlman[3], Charles A. Padgett[1,2], and George Chartas[4]
[1] Department of Physics, University of Maryland, Baltimore County, 1000 Hilltop Circle, Baltimore, MD 21250, USA
[2] NASA Goddard Space Flight Center, Code 663, Greenbelt, MD 20771, USA
[3] Department of Physics and Space Sciences, Florida Institute of Technology, 150 West University Boulevard, Melbourne, FL 32901, USA
[4] Department of Astronomy and Astrophysics, Penn State University 525 Davey Lab, University Park, PA 16802, USA
Received 2008 May 24; accepted 2008 September 5; published 2008 December 30

ABSTRACT

We present new Near-Infrared Camera and Multi-Object Spectrometer and attitude control system observations of the quasar jet PKS 0637-752, and we use them, together with existing multiwavelength observations, to produce the most complete spectral coverage of the source to date. We explore the implications of these observations in the context of models for the jet X-ray emission. By relaxing the assumption of equipartition, we undertake an exhaustive study of the parameter space for external Compton off the cosmic microwave background (CMB) (EC/CMB) model. We find that the multiwavelength observations exclude a magnetic-field-dominated jet. Using the method proposed by Georganopoulos et al. for probing the jet matter content, we show that protons are practically needed for all jet configurations, extending a previous application of the method by Uchiyama et al. that was based on exploring three particular jet configurations. We also show that equipartition is the only configuration that can reproduce the observations and have one proton per radiating lepton. We finally present a rather model-independent argument that the jet has a spine-sheath flow pattern, with the spine being faster and emitting most of the infrared-optical X-ray emission.

Key words: galaxies: jets – infrared: galaxies – quasars: individual (PKS 637, 752) – radiation mechanisms: non-thermal

Online-only material: color figures

1. INTRODUCTION

When the *Chandra X-Ray Observatory* used the bright X-ray quasar PKS 0637-752 to focus its mirror assembly during its first observation, astronomers expected to detect a bright X-ray point source. However, in addition to the bright core of the quasar, *Chandra* detected significant X-ray emission from the previously-detected quasar radio jet (Schwartz et al. 2000; Chartas et al. 2000). This bright X-ray emission was found to overproduce the X-ray flux that corresponds to the extension of the radio-optical spectrum to X-ray energies, arguing for a second spectral component, for which the most plausible candidate was initially thought to be synchrotron-self-Compton (SSC) emission. However, it became immediately apparent from modeling the multi-wavelength spectral energy distribution (SED) of the knots of PKS 0637-752 that the expected SSC X-ray flux under equipartition conditions severely underpredict the observed X-ray flux, with the case for SSC only getting worse when relativistic beaming effects are considered (Schwartz et al. 2000; Chartas et al. 2000).

Following the discovery of the X-ray jet of PKS 0637-752, there has been extensive observational and theoretical work on powerful quasar jets (for a recent review, see Harris & Krawczynski 2006). Further X-ray studies using *Chandra* have confirmed that bright X-ray-emitting jets are common among radio-loud quasars and radio galaxies (e.g., Sambruna et al. 2002, 2004, 2006; Marshall et al. 2005; Siemiginowska et al. 2002; Kataoka et al. 2003; Jorstad & Marscher 2004; Cheung et al. 2006; Schwartz et al. 2006). They also confirmed that in these jets, the X-ray emission is a spectral component separate from the radio-optical synchrotron emission, with the X-ray flux being higher that that anticipated by simply extending the radio-optical spectrum to X-ray energies.

A plausible candidate for the X-ray emission mechanism was suggested by Tavecchio et al. (2000) and Celotti et al. (2001). These authors argued that the X-ray flux of the knots of PKS 0637-752 is due to external Compton emission from jet relativistic electrons in equipartition with the magnetic field of the jet, up-scattering cosmic microwave background photons (EC/CMB). The model, motivated by the superluminal motions observed in the subparsec(sub-pc) scale jet (Lovell et al. 2000), requires that (1) the large-scale jet is significantly beamed (bulk Lorentz factor $\Gamma \sim 10$) and (2) the electron distribution has a low-energy break or cutoff at $\gamma \lesssim 100$. Both of these requirements increase the required jet power uncomfortably close to the Eddington limit (Dermer & Atoyan 2004). Because in the EC/CMB model the X-rays are produced by very low-energy electrons ($\gamma \sim 100$), these electrons have long cooling times that allow them to reach the terminal points of even megaparsec scale jets without losing a significant fraction of their energy. Thus, in the EC/CMB, we would expect to see continuous X-ray emission throughout the jet instead of the knotty X-ray structure we usually observe. A possible solution to this issue is to assume that jets are not continuous and that the X-ray knots are ejected from the central engine during periods of high activity and retain their knot structure as they propagate downstream. Also, in several X-ray jets, the ratio of the radio to X-ray flux in the knots decreases as we move away from the core. In the context of the EC/CMB model, this can be explained if jets gradually decelerate (Georganopoulos & Kazanas 2004). In some jets, including PKS 0637-752, there is a low emission bridge of ∼5–10 arcsec connecting the quasar core to the first jet knot. Georganopoulos et al. (2005) argued

that, in the context of the EC/CMB model, this can be used to constrain the matter content of the jet through infrared (IR) observations of the bridge, and Uchiyama et al. (2005) used this to show, through *Spitzer* observations of PKS 0637-752, that an electron–positron jet is not favored if the X-rays are due to the EC/CMB mechanism.

The fact that the EC/CMB model requires bulk Lorentz factors much in excess than those required by jet-to-counterjet radio asymmetry arguments (e.g., Arshakian & Longair 2004), together with the issues just discussed, raises the possibility that the X-rays are of synchrotron nature (e.g., review by Harris & Krawczynski 2006) by an additional population of very high-energy (∼100 TeV) electrons. Such high-energy electrons may be produced if the jet is characterized by velocity shear (Stawarz & Ostrowski 2002; Rieger & Duffy 2004). Alternatively, the decay of a collimated neutron beam produced in the sub-pc scale jet can provide a second high-energy electron component (Atoyan & Dermer 2004). The synchrotron option is viable for sources such as 3C 273, for which the high-energy component extends smoothly down to optical energies (Uchiyama et al. 2006; Jester et al. 2006, 2007), but runs into difficulties for sources such as PKS 0637-752, in which the high-energy component cuts off before the optical regime, because these high-energy electrons would rapidly cool to lower energies and would radiate in the optical, producing, thereby, a much higher optical flux than observed. If, indeed, the X-ray emission is of synchrotron nature, the multi-TeV electrons responsible for it will unavoidably up-scatter the CMB photons to TeV energies (Georganopoulos et al. 2006). For 3C 273, the upper limit from shallow HESS TeV observations is compatible with the synchrotron interpretation, provided $\delta \lesssim 10$, where δ is the usual Doppler factor.

Here, we present *Hubble Space Telescope* (*HST*) Near-Infrared Camera and Multi-Object Spectrometer (NICMOS) and Advanced Camera for Surveys (ACS) observations of PKS 0637-752, and discuss the constraints they pose, together with available multiwavelength observations, on our understanding of the jet physics. In Section 2, we present the data reduction procedure; in Section 3, we present our observational results, together with existing multiwavelength observations; in Section 4 the constraints on the jet physics are presented; and in Section 5, our conclusions are given.

2. OBSERVATIONS AND DATA REDUCTION

PKS 0637-752 ($z = 0.651$, luminosity distance $d_L = 3895$ Mpc) has been observed in different energy bands by other researchers. Here we use the 8.6 GHz radio observations taken with the Australia Telescope Compact Array (ATCA; Lovell et al. 2000), the *Spitzer* observations by Uchiyama et al. (2005), the *HST* Wide Field Planetary Camera 2 (WFPC2) observations by Schwartz et al. (2000), and the *Chandra* X-ray observations by Chartas et al. (2000) and Schwartz et al. (2000).

Our *HST* observations took place on 2005 November 15 and 16 using the ACS and NICMOS instruments, respectively. The data were processed by the standard "on-the-fly" reprocessing calibration pipeline. We performed subsequent data reduction using the National Optical Astronomy Observatory (NOAO) Image Reduction Analysis Facility (IRAF) and Python IRAF (PyRAF) packages. The ACS data were taken using filter F475W and the Wide Field Channel (WFC) detector, which has a pivot wavelength of 0.4744 μm with a field of view (FOV) of $202'' \times 202''$, corresponding to a resolution of 0.05 arcsec/pixel. The total exposure time was 2556 s. These data were reduced using the standard "multidrizzle" script, which completes all the data reduction and dithering tasks. These tasks include creating a bad pixel map, sky subtraction, drizzling the data onto separate output images, combining the output images into a median image, blotting or undrizzling the combined image, creating a cosmic ray mask by comparing the blotted image to the original images, and drizzling all the images onto a final mosaic by using the bad pixel and cosmic ray masks.

The NICMOS data were taken using the nonlinear inverse Compton 3 (NIC3) camera using filter F160W with a pivot wavelength of 1.604 μm. The FOV of the NIC3 camera is $51\farcs2 \times 51\farcs2$ with a resolution of $0\farcs2$/pixel. Although it has a lower angular resolution, we used the NIC3 camera instead of the NIC1 or NIC2 as the NIC3 camera has larger pixels, which would help us detect any faint, extended emission from the cold electrons in the jet. The NICMOS observations were split into three orbits, each with an exposure time of 3072 s. Orbits 2 and 3 were shifted by 5 and 10 pixels, respectively. This enables us to detect hot pixels and other CCD defects easily. In the NICMOS data, we come across some important anomalies, such as the pedestal effect and bad pixels, which are not corrected for by multidrizzle. The pedestal effect is corrected for by "pedsub"; hot pixels were replaced by the average value of the surrounding pixels using the "imedit" task. We could not use the "multidrizzle" task as it does not account for the pedestal effect, and tended to oversubtract the sky for the NICMOS data. The compensation was done by using tasks from the "dither" package in IRAF. These tasks included sky subtraction, drizzling the data with corrections for geometric and other distortions by the CCD, correcting for the shifts in images from the three orbits, and rotating the images to show north up and east left.

3. RESULTS

The radio jet (8.6 GHz, taken with the ATCA; Lovell et al. 2000), shown by the contours in Figure 1, shows a bright jet extending to $\sim 10''$ from the quasar core, and then bending northwest. There is also a counterjet radio feature approximately $8''$–$9''$ east of the core and at least two knots between $7''$ and $10''$ west of the core with possible features further in. The *Chandra* X-ray image (Chartas et al. 2000; Schwartz et al. 2000) shows at least three X-ray knots, WK 5.7, WK 7.8, WK 8.9, and, possibly a fourth knot, WK 9.7. Previous *HST* observations (WFPC2, F702W) at an effective wavelength 0.697 μm (Schwartz et al. 2000) detect the three knots WK 5.7, WK 7.8, WK 8.9. There was also a deeper by a factor of ∼2 Space Telescope Imaging Spectrograph (STIS) *HST* observation (PI C. M. Urry, cycle 10) practically at the same effective wavelength. The IR (*Spitzer*) jet (Uchiyama et al. 2005) is well aligned with the X-ray and radio jet and shows two bright knots: WK 7.8 and WK 8.9. However, the resolution of *Spitzer* makes it difficult to distinguish these knots clearly. There is no evidence of the jet after the bend or the counterjet radio feature in the *Spitzer* and *Chandra* data.

From both the ACS and NICMOS images, we see the bright quasar core and the three bright knots WK 7.8, WK 8.9, and WK 9.7 separately, with WK 8.9 being the brightest knot. In the NICMOS image, we also see the inner knot WK 5.7, which was only seen in X-rays before, and we obtain limits from NICMOS and ACS for the counterjet radio feature. Due to the lower spatial resolution of the NIC3 camera, there is contamination from a background galaxy from the south in the WK 8.9 knot (this galaxy is also seen on the ACS image). The host galaxy contamination is accounted for by subtracting the galaxy flux, scaled by the ratio of the two areas, from the raw flux. The higher

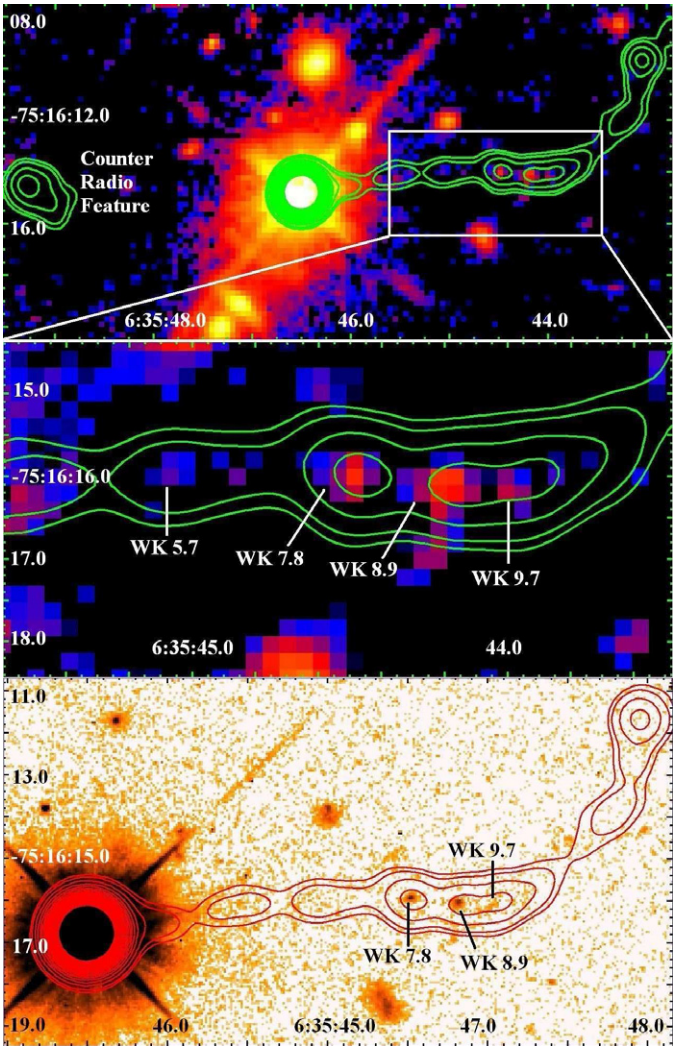

Figure 1. The NICMOS and ACS images with the radio contours for PKS 0637-752 overlaid. The top panel is the NICMOS image of the whole jet with green radio contours. The middle panel is a zoomed image of the white box in the top panel. The bottom panel shows the ACS image with radio contours in red.

(A color version of this figure is available in the online journal.)

resolution of the ACS camera helps prevent such contamination in the ACS image.

The optical jet is well aligned with the radio, X-ray, and IR jet. We do not detect the jet after the bend and the counterjet radio feature in both the ACS and NICMOS images, respectively. With ACS, we see that WK 7.8 and WK 8.9 are well-confined bright knots whereas WK 9.7 seems to be extended in the northwest direction. With NICMOS, we also detect a previously-undetected feature along the jet between WK 5.7 and WK 7.8. This new feature (WK 6.3) is approximately 6.″3 from the core and is the least bright feature from all the knots or features we detect. Both WK 5.7 and WK 6.3 are enveloped by the same radio feature, and could not have been resolved by the *Spitzer* observations. For this reason, and to allow direct comparison with Uchiyama et al. (2005), in the rest of the paper we use the same size they used for the WK 5.7 knot, which includes the WK 6.3 feature. It is interesting to note that even though the brightest pixels in NICMOS do fall within the radio knots, there are parts of knots that lie slightly outside the contours. This may suggest a slight shift in the overall knot position between the optical and radio knots. The higher-resolution ACS knots, however, fall well within the radio contours.

The SEDs for the four knots (WK 5.7, 7.8, 8.9, and 9.7) are shown in Figure 2. We see that all the knots have the same basic shape of dropping significantly in the optical before brightening in the X-rays. The three near-IR (NIR) optical points (NICMOS, WFPC2, and ACS) are interesting as they are the interface between the radio-to-optical component and the optical-to-X-rays component of the SED. An interesting question is if in the tail of the optical component can one discern the rise of the new component that eventually produces the X-rays. For knot 8.9, there is no evidence for this, as we see the point-to-point slopes between the three points drop. Knot WK 7.8 shows an interesting trend near the ACS point. The point-to-point slopes between the NICMOS-WFPC2 points and the WFPC2–ACS points are beyond 3σ of each other: $\alpha_{\rm NICMOS-WFPC2} = -0.907 \pm 0.055$ and $\alpha_{\rm WFPC2-ACS} = -0.345 \pm 0.119$, respectively. However, the probability of the three points falling on a line, using the χ^2 test, is 0.15. Thus, knot 7.8 shows suggestive, but not conclusive, evidence of an additional component in the ACS frequency range. Knot 9.7 clearly shows the presence of an additional component as the ACS flux is approximately the same as the WFPC2 flux. Interestingly, we see that the brightest knot shows the least evidence for this component while the least bright knot gives a strong evidence for the same. The SED for the total western jet and the SED for the counterjet radio feature are shown in Figure 3. The flux of the total jet is calculated by adding up all the definitive fluxes from the four knots (WK 5.7, 7.8, 8.9, 9.7). The fluxes with limits were ignored so as to obtain a lower limit on the total jet flux. The complete list of fluxes is given in Table 1.

4. CONSTRAINTS ON THE JET PHYSICS

4.1. The Synchrotron X-ray Interpretation

A possibility mentioned in Section 1 is that the X-ray emission for knots with a broadband SED similar to that of knot WK 7.8, in which the X-rays are part of a separate spectral component, is of synchrotron nature (Hardcastle et al. 2004; Harris & Krawczynski 2006; Jester et al. 2007). A typical one-zone synchrotron model in which the electron distribution is regulated by injection, radiative losses, and escape runs into difficulties because the X-ray emitting electrons have a cooling time, significantly faster than their escape time. The observed X-ray spectral index $\alpha_X \approx 0.7$ requires an electron energy distribution (EED) that locally is a power law $n(\gamma) \propto \gamma^{-p}$, with $p = 2\alpha_X + 1 = 2.4$. Because these multi-TeV energy electrons are in the fast cooling regime, the acceleration mechanism that produced them is required to provide an EED $n(\gamma) \propto \gamma^{-1.4}$. Such hard EEDs are far from the usual 2–2.3 index of shock acceleration (Kirk et al. 2000), although an index of 1.4 is within the wide range anticipated in different acceleration scenarios (e.g., Ostrowski 2008). A more serious issue with one-zone models is the fact that the level of the observed optical-UV emission is very low compared to the extrapolation of the X-ray emission in the optical. This is not expected, because radiative cooling should have extended the high-energy electron population to lower energies, and these lower energy electrons would fill the optical-UV "valley" with their synchrotron emission. Two-zone synchrotron models can be devised, at the cost of practically doubling the free parameters. In two-zone models where the acceleration of the X-ray emitting particles takes place in a separate zone, the optical "valley"

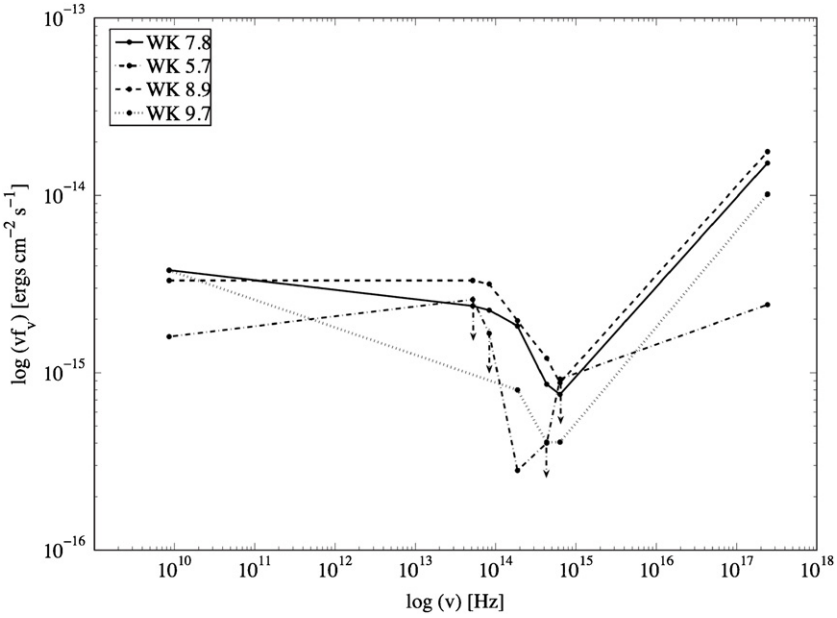

Figure 2. The SEDs of the four knots seen in the western jet for PKS 0637-752. The arrows represent upper limits in the SED for knot WK 5.7. The connecting lines are drawn to guide the eye.

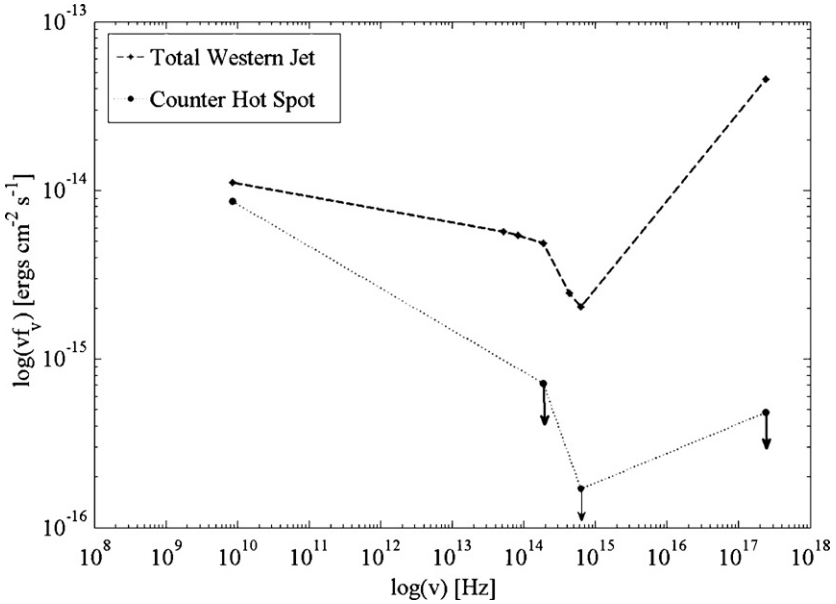

Figure 3. A comparison between the SED of the total western jet (WK 7.8 + WK 8.9 + WK 9.7) and that of the total eastern jet, noted as the counter radio feature in Figure 1. Note that while the radio fluxes are comparable, there are only upper limits for the optical and X-ray emission of the eastern jet. As we argue in Section 4.6, this suggests a spine-sheath flow with the spine being faster and emitting most of the IR to X-ray radiation.

Table 1
Flux Densities of the Various Parts of PKS 0637-752

Telescope	Frequency (Hz)	WK 5.7	WK 7.8	WK 8.9	WK 9.7	Total Western Jet*	Counterjet Feature
ATCA	8.60×10^{9}	1.60×10^{-15}	3.78×10^{-15}	3.31×10^{-15}	3.72×10^{-15}	1.12×10^{-14}	8.60×10^{-15}
Spitzer	5.17×10^{13}	$2.59 \times 10^{-15}_{L}$	2.38×10^{-15}	3.31×10^{-15}	...	1.07×10^{-14}	...
Spitzer	8.33×10^{13}	$1.67 \times 10^{-15}_{L}$	2.25×10^{-15}	3.17×10^{-15}	...	8.75×10^{-15}	...
HST/NICMOS	1.87×10^{14}	2.81×10^{-16}	1.83×10^{-15}	1.96×10^{-15}	7.99×10^{-16}	4.88×10^{-15}	$1.68 \times 10^{-15}_{L}$
HST/WFPC2	4.30×10^{14}	$4.00 \times 10^{-16}_{L}$	8.61×10^{-16}	1.21×10^{-15}	4.05×10^{-16}	2.87×10^{-15}	...
HST/ACS	6.32×10^{14}	$9.21 \times 10^{-16}_{L}$	7.54×10^{-16}	8.77×10^{-16}	4.05×10^{-16}	2.96×10^{-15}	$1.69 \times 10^{-16}_{L}$
Chandra	2.42×10^{17}	2.42×10^{-15}	1.52×10^{-14}	1.77×10^{-14}	1.02×10^{-14}	4.55×10^{-14}	$4.84 \times 10^{-16}_{L}$

Notes. The errors in the NICMOS and ACS fluxes are 5% of the flux value. The radio data are taken from Lovell et al. (2000), the *Spitzer* from Uchiyama et al. (2005), and the X-rays from Chartas et al. (2000) and Schwartz et al. (2000).

[a] The fluxes given here are in units of ergs cm^{-2} s^{-1}.

* Total Western Jet = WK 5.7 + WK 7.8 + WK 8.9 + WK 9.7.

[L] Upper limit.

forces us to adopt an ad-hoc injection of electrons at ∼10 TeV energies which are then accelerated up to at least ∼100 TeV before they escape. This population of electrons must then escape to an environment of much lower magnetic field, so that these electrons will not produce substantial optical-UV synchrotron emission as they cool.

4.2. Bulk Compton Constraints on the Cold Lepton Power

As proposed by Georganopoulos et al. (2005), the fact that the IR emission of the "bridge," the part of the jet interior to knot WK 7.8, is very low can be used to derive constraints for the lepton power carried by the jet, under the assumption that the jet power in the bridge is carried by some combination of protons and leptons and that the jet flow is not episodic. The idea behind the bridge diagnostic is that even if the electrons are cold ($\gamma \approx 1$) in the bulk flow frame, they will up-scatter the CMB to higher energies due to their bulk motion. The power in the lepton beam is then constrained by the requirement that the bulk Compton (BC) emission should not overproduce the upper limits of the bridge emission. Furthermore, the cold lepton power constraints can be used in the context of the EC/EMB model for the nonthermal knot emission to constrain the jet matter content: a knot configuration that successfully produces the knots' SED will be incompatible with an electron–positron jet if the lepton power required to be fed into the knot exceeds the BC upper limit on the power carried by leptons in the bridge. This was applied by Uchiyama et al. (2005) on PKS 0637-752 using *Spitzer* observations to argue that, in the context of the EC/CMB model, the three jet configurations they considered are incompatible with an electron–positron jet, because the power required to be fed into the knot exceeds the upper limit of the power carried by leptons.

We calculate here the model-independent constraints for the cold lepton power, applying the formalism of Georganopoulos et al. (2005) to our 1.6 μm NICMOS data of WK 5.7, as well as the *Spitzer* data at 3.6 μm and 5.8 μm (as it turns out, shorter wavelength limits do not constrain the power further as long as the bulk Lorentz factor $\Gamma \gtrsim 20$). A beam of cold electrons of power L_e that propagates a length l with a bulk Lorentz factor Γ and velocity $u = \beta c$ through a blackbody photon field characterized by a temperature T produces a specific luminosity

$$L_\nu = \frac{L_e \sigma_T l k T}{m_e c^5 \beta^2 \Gamma^3}\, \nu^2 \ln\left[\frac{1-\exp[-h\nu\Gamma(1+\beta)/(\delta\, kT)]}{1-\exp[-h\nu/(\Gamma\delta\, kT(1+\beta))]}\right], \quad (1)$$

where $\delta = 1/(\Gamma(1-\beta\cos\theta))$ and θ is the angle between the beam and the line of sight (LOS). By selecting the knot WK 5.7 (Uchiyama et al. 2005) and setting the length to $l = 13.8/\sin\theta$ Kpc, we require that L_ν is smaller than the WK 5.7 knot upper limits and calculate the upper limit for L_e. The results are plotted in Figure 4 for three different angles (for $\theta < 4^\circ$, the jet becomes longer than 1 Mpc; $\theta \gtrsim 8^\circ$ is in disagreement with the superluminal motions observed in the VLBI core, unless the jet is significantly bend) and for a range of Γ. We see that for a given angle, for $\Gamma \gtrsim 10$, the constraints are relatively flat with increasing Γ, going from $\sim 10^{45}$ erg s^{-1} for $\theta = 4^\circ$ to $\sim 10^{47}$ erg s^{-1} for $\theta = 8^\circ$. If we assume a black-hole mass of $10^9\ M_\odot$, this suggests that for all plausible angles, the cold lepton power has to be sub-Eddington as long as $\Gamma \gtrsim 10$. We discuss the implications of these constraints on the EC/CMB model in Section 4.4.

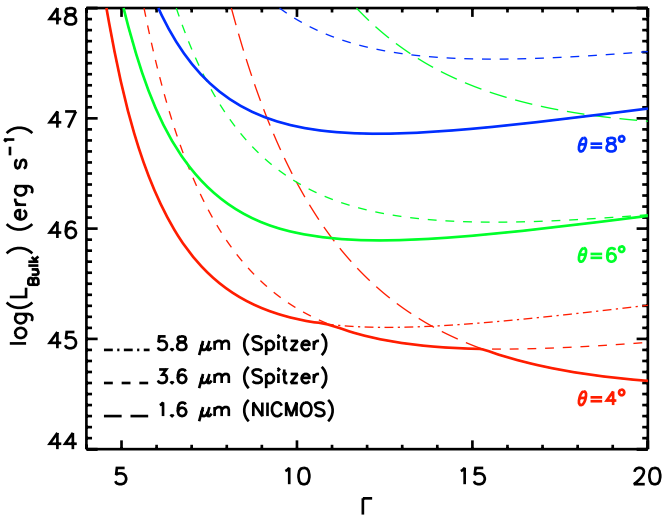

Figure 4. The solid lines are upper limits on the bulk power of cold leptons in the jet for three different angles, as a function of the bulk Lorentz factor Γ. These solid lines are the lower envelope of constraints derived from the upper limits on the flux of knot WK 5.7 through *Spitzer* (Uchiyama et al. 2005) observations at 5.8 μ, (dot-dash lines), 3.6 μm (long dash line), and NICMOS observations at 1.6 μm (short dash line).

(A color version of this figure is available in the online journal.)

4.3. Why the Magnetic Field Cannot Dominate in the EC/CMB Model

We now turn to the more constrained EC/CMB model, focusing our attention on knot WK 7.8, which we model as a sphere of radius $R = 1$ kpc (corresponding to an angular diameter of 0.3 arcsec) permeated by a magnetic field B. We assume that the EED, at least in the regime responsible for the synchrotron radio and EC/CMB X-rays, is a power law $N(\gamma) = k\gamma^{-p}$, where $N(\gamma)d\gamma$ is the total number of electrons in the source with Lorentz factors in the range γ, $\gamma + d\gamma$. Using the δ-function, energy-conserving approximations for the synchrotron, and IC emissivities, the EC/CMB and synchrotron-observed specific luminosity ($L_{\rm EC}$ and $L_{\rm S}$, respectively) can be written as

$$L_{\rm EC}(\nu) = c_1 k \delta^{4+2\alpha}\nu^{-\alpha}, \qquad L_{\rm S}(\nu) = c_2 k B^{\alpha+1}\delta^{3+\alpha}\nu^{-\alpha}, \quad (2)$$

where $\alpha = 2p+1$, δ is the usual Doppler factor and c_1, c_2 are listed in the appendix. The magnetic field energy density is a fraction f of the radiating lepton energy density:

$$\frac{B^2}{8\pi} = f\,\frac{3km_ec^2\gamma_{\rm min}^{1-2\alpha}}{4\pi R^3}, \quad (3)$$

where $\gamma_{\rm min}$ is the low-energy cutoff of the EED and, in agreement with the radio and X-ray observations, we have assumed $p > 2$.

Although equipartition ($f = 1$) is widely adopted in the study of jets, there is no physical argument for why the plasma should be in equipartition. Here, and in the rest of this work, instead of presuming equipartition, we let f be a free parameter and we examine how it can be constrained. For a given value of f, the above three equations can be solved to provide B, δ, and k. For a given resulting δ, the maximum angle $\theta_{\rm max}$ that the jet can form with the LOS is $\sin^{-1}(1/\delta)$. We constrain the jet orientation angle to $4^\circ < \theta < 9^\circ$, with the lower limit set by the requirement that the jet up to knot WK 9.7 is less than 1 Mpc long, and the upper limit set by the observed superluminal core speeds (Lovell et al. 2000). As can be seen in Figure 5, magnetically-dominated

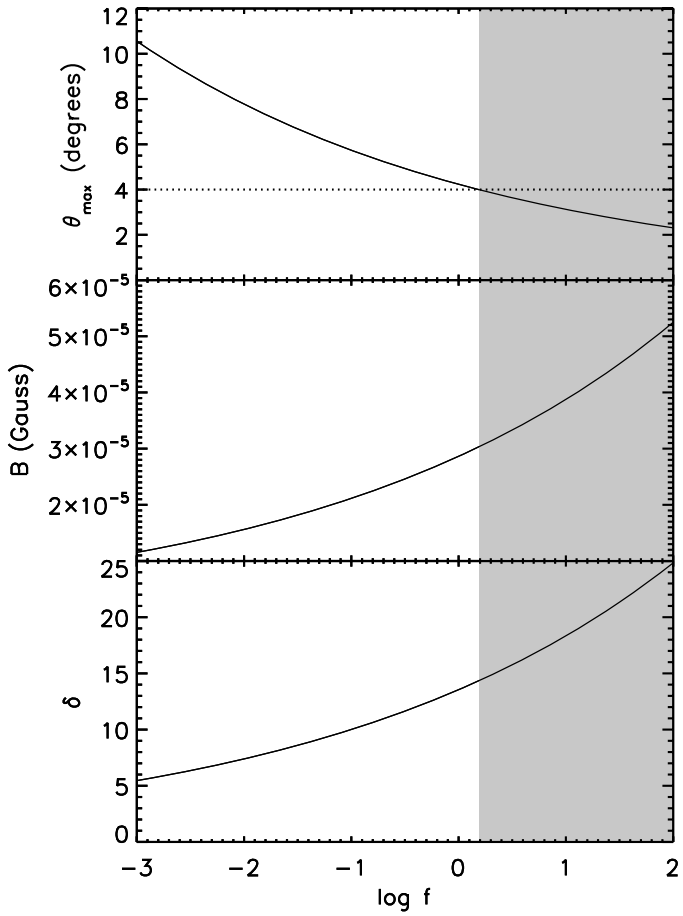

Figure 5. The Doppler factor δ (bottom panel), the magnetic field B (middle panel), and the maximum permitted angle $\theta_{\rm max}$ (top) as a function of $f = U_B/U_{\rm part}$, the magnetic field to radiating particle energy density. The shaded area corresponds to $\theta_{\rm max} < 4^\circ$ that requires jets longer than 1 Mpc. In this calculation, we assumed $\gamma_{\rm min} = 20$. This can vary by at most ±50% without violating the optical and X-ray constraints (higher values underproduce the X-rays; lower values overproduce the optical). Such variations move the curves somewhat but do not change our results significantly.

jets ($f \gtrsim 1$) are excluded, because they require $\theta_{\rm max} < 4^\circ$. Jets in which the radiating lepton energy density is increasingly higher than that of the magnetic field require gradually smaller δ and larger $\theta_{\rm max}$.

4.4. Matter Content in the EC/CMB Model

We study here the constraints imposed on the plasma composition and Lorentz factor of the jet by the requirement that any viable configuration should reproduce the SED of knot WK 7.8 (hereafter, simply called the knot) and should not be substantially super-Eddington. Given that the plasma is not magnetically dominated, we only examine solutions with $f \lesssim 1$. For a given jet orientation angle θ, there are two possible values of the bulk Lorentz factor Γ compatible with a particular δ:

$$\Gamma_{1,2} = \frac{1 \pm (1 - (1 - \cos^2\theta)(1 + \cos^2\theta\,\delta^2))^{1/2}}{\delta(1 - \cos^2\theta)}. \quad (4)$$

Selecting three representative angles ($\theta = 4^\circ, 6^\circ, 8^\circ$), we let f vary, and for each f, we calculate δ and B. For each value of δ, we calculate the two possible values of Γ. A constraint on Γ can be imposed by the requirement that the electrons responsible for the radio emission escape from the knot before they have time to cool, as suggested by the overall SED of the knots and from the fact that the radio spectrum of the knots has a spectral index $\alpha_r \approx 0.8$ that corresponds to an EED electron index of $p = 2\alpha_r + 1 \approx 2.6$, typical of uncooled electrons in radio sources. The requirement that cooling does not affect the radio frequencies can be written as $\nu_c > 10^{10}$ Hz, where the cooling frequency is

$$\nu_c = \frac{e}{2\pi m_e}\left[\frac{9 m_e c^2}{16\,\sigma_\tau k\, R\, U_{\rm CMB}(1+z)^4\,\Gamma^2}\right]^2 \frac{B\delta}{1+z}, \quad (5)$$

with k being the escape time from the source in units of light crossing time ($k = 3$ is in agreement with the jump conditions at highly relativistic shock; Blandford & McKee 1976), $U_{\rm CMB}$ the CMB energy density, σ_τ the Thomson cross-section, and z the redshift of the source (this equation does not take into account synchrotron losses that turn out to be negligible compared to the EC/CMB ones, as can be seen by the fact that the X-ray luminosity is higher than the radio optical). We plot the two different Γ-branches for each angle at the lower panel of Figure 6, taking into account the above constraint, which, for the range of f we consider, only affects the fast Γ branch for $\theta = 4^\circ, 6^\circ$ (without this constraint, these upper branches would continue toward higher values of Γ and lower values of f. As can be seen, if we drop the equipartition assumption, a wide range, $3 \lesssim \Gamma \lesssim 28$, can reproduce the X-ray and radio data.

An additional strong constraint comes from the requirement that the SED breaks from the radio slope at $\sim 10^{11}$ Hz, peaks at $\sim 10^{12}$ Hz, and curves down at IR, optical, and UV bands (Uchiyama et al. 2005; also see Section 4.5). The most plausible explanation for this break is radiative cooling. Using Equation (5) for $\nu_c = 10^{11}$ Hz, in the lower panel of Figure 6, we plot with a solid black line the locus of configurations with $\nu_c = 10^{11}$ Hz. This line intersects the upper Γ branch for all angles. Numerical models that fit the knot SED should cluster around this line (see Section 4.5). If, however, we choose to interpret the SED not as due to radiative cooling, but rather as due to an injected EED that is intrinsically curved, then all the configurations below the black line are possible.

We now turn to the question of the power required to feed the knot, noting that power requirements significantly higher than the Eddington luminosity of a $\sim 10^9\ M_\odot$ black hole ($L_{\rm Edd,9} = 1.38 \times 10^{47}$ erg s^{-1}) are unpleasant, and power requirements higher than the Eddington luminosity of a $\sim 10^{10}\ M_\odot$ black hole are disfavored. The power in radiating leptons and magnetic field required to feed the knots is

$$L_{e^- - e^+} = \pi R^2 \beta c \Gamma^2 U_B (1 + 1/f). \quad (6)$$

In the second from the bottom panel of Figure 6, we plot (green lines) the jet power required to be fed into the knot in the case of an e^-–e^+ jet composition for the lower Γ-branch (as we mentioned above these configurations are plausible only if we presume that the shape of the SED is not due to cooling, but rather due to an appropriately fine-tuned intrinsically curving EED). The required power is for all cases below $L_{\rm Edd,9}$ (the lightly shaded area indicates $L_{\rm jet} > L_{\rm Edd,9}$, while the heavily shaded area indicates $L_{\rm jet} > L_{\rm Edd,10}$). We also plot with red lines the upper limit to the jet power from the constraint that BC emission cannot overproduce the flux limits of knot WK 5.7. As can be seen, the only part of the parameter space that a leptonic configuration is unattainable (red line lower than green) and

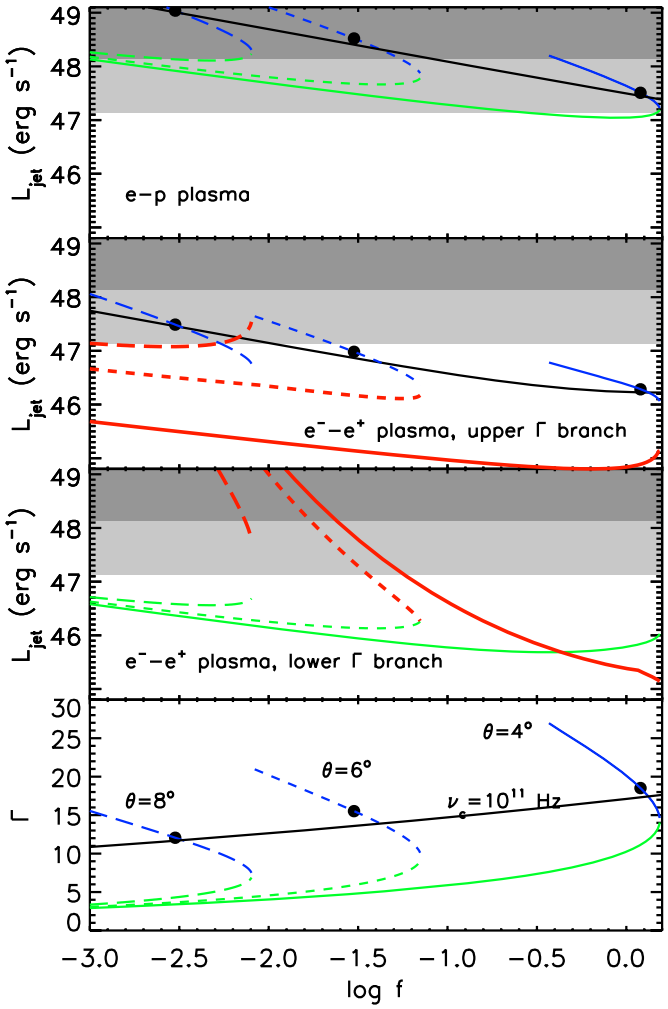

Figure 6. Bottom panel: for three different angles, we plot, as a function of f, the lower (green) and upper (blue) Lorentz factors Γ that are compatible with the radio and X-ray observations of knot WK 7.8 in the EC/CMB model. We also plot with a black line the locus of the models that have a synchrotron cooling break frequency $\nu_c = 10^{11}$ Hz. The black line has the same meaning in the top two panels. The filled circles correspond to numerical models we discuss in Section 4.5. Second from the bottom panel: the power required for e^-–e^+ jets (green lines) and the upper limits of the cold lepton jet power from the BC constraints (red lines), both in the lower Γ-branch configurations. The shaded areas correspond to $L_{\rm jet} > L_{\rm Edd,9}$ (light gray shade) and $L_{\rm jet} > L_{\rm Edd,10}$ (heavy gray shade). Second from the top panel: the power required for e^-–e^+ jets (blue lines) and the upper limits of the cold lepton jet power from the BC constraints (red lines), both in the upper Γ-branch configurations. Shaded areas in this and the next panel are the same as in the previous panel. Top panel: the jet power in the case of an e–p jet for the lower (green) and upper (blue) Γ branches. The three different line styles refer to the three different angles. The same style of the lines is used in all plots for each angle.

(A color version of this figure is available in the online journal.)

therefore a proton contribution is needed, is for configurations close to equipartition.

In the second from the top panel we plot the same quantities for the upper Γ-branch, that includes the more plausible configurations in which the SED shape is due to self-consistent radiative cooling (black line). Except for the high f tail of large angle models (in the case depicted, $\theta = 8^\circ$ models with $\log f \approx -2.1$), the rest of the e^-–e^+ models are excluded because they require more power in the knot than allowed by the upper limit set by the BC constraints (red lines below blue lines). This means that these models are viable only if protons carry a power at least equal to the difference between that required by the knot and

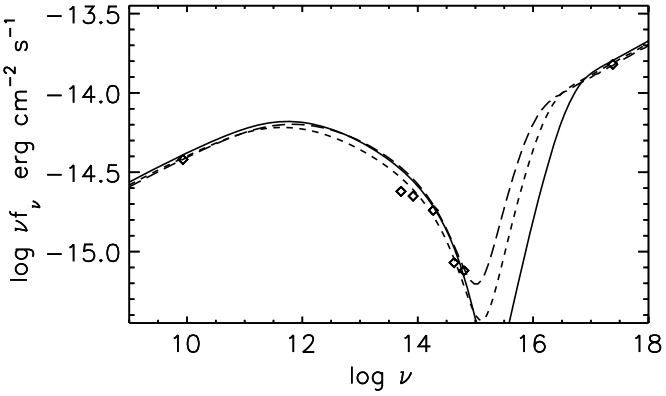

Figure 7. The data (solid points; see Table 1) and three model SEDs for knot WK 7.8 at $\theta = 4^\circ$ (solid line), $\theta = 6^\circ$ (short dash line), $\theta = 4^\circ$ (long dash line). In all three models, $\gamma_{\rm min} = 20$, while $\gamma_{\rm max} = 10^6$, 1.5×10^6, 2×10^6 for the solid, short, and long dash lines, respectively, chosen by the requirement to fit the optical-UV tail of the synchrotron emission.

that carried by the cold leptons in the bridge. Note that large angles are disfavored because $L_{\rm jet} \gtrsim L_{\rm Edd,9}$.

A particular e–p jet is one in which for every radiating lepton, there is a cold proton. The jet power required in such a jet is

$$L_{e-p} = \pi R^2 \beta c \Gamma^2 U_B \left[1 + \frac{1}{f}\left(1 + \frac{m_p}{m_e \langle\gamma\rangle}\right)\right],$$
$$\langle\gamma\rangle = \frac{\gamma_{\rm min}(p-1)}{p-2}. \quad (7)$$

We plot this power in the upper panel of Figure 6, together with the black lines of models with $\nu_c = 10^{11}$ Hz, and we note that the only models that do not have extreme power requirements ($L_{\rm jet} \lesssim L_{\rm Edd,9}$) are those close to equipartition (and, by necessity, at a small angle).

To sum it up, under the most plausible assumption that the shape of the SED is due to electron cooling, e^-–e^+ jets are excluded. Assuming a minimal contribution of protons, just enough to power the knot, higher-angle jets are disfavored because they require $L_{\rm jet} \gtrsim L_{\rm Edd,9}$. Increasing the proton contribution to one proton per radiating electron increases the jet power, and the only configurations that have $L_{\rm jet} \sim L_{\rm Edd,9}$ are those at equipartition and, consequently, a small angle.

4.5. Model SEDs

To confirm that models on or close to the black lines of Figure 6 provide reasonable representations of the knot SED, in Figure 7, we present the results of three simulations[5] at angles $\theta = 4^\circ, 6^\circ, 8^\circ$. For each angle, we select a corresponding $f = 1.2, 0.03, 0.003$, and from these two parameters, we calculate the rest of the model parameters from Equations (2)–(4) and (6) (see Table 2). In Figure 6, we also plot with solid circles the location of the models. All three models provide adequate representations of the SED and are, therefore, equally acceptable. As expected, all three models are located close to the black line of $\nu_c = 10^{11}$ Hz. Also, all three models require protons to carry some ($\theta = 8^\circ$) or most ($\theta = 4^\circ, 6^\circ$) of the power. Only the model close to equipartition ($\theta = 4^\circ$), however, can have one proton per radiating particle and still be sub-Eddington.

[5] The code can be found at http://jca.umbc.edu/~markos/cs.

Table 2
Parameters for the SED Models

θ	f	B (10^{-5} G)	δ	Γ	$L_{e^- - e^+}$ (erg s^{-1})	L_{e-p} (erg s^{-1})
4°	1.2	2.9	13.9	18.5	1.9×10^{46}	3.2×10^{47}
6°	0.03	1.8	8.5	15.5	9.6×10^{46}	3.3×10^{48}
8°	0.003	1.3	6.3	12.7	3.1×10^{47}	1.1×10^{49}

Note. θ and f are the free parameters.

4.6. A High-Energy Faster Spine and a Low-Energy Slower Sheath

Having exhausted the constraints that can be imposed on the jet physics in the context of the EC/CMB model, we now present a rather model-independent argument that the jet of PKS 0637-752 is characterized by a fast spine emitting most of the IR to X-ray emission, and a slow sheath emitting most of the radio. The first direct observational argument that a radio jet may be characterized by a fast spine and a slower sheath came from radio observations of the several-kpc radio jets of the FR II radio galaxy 3C 353 by Swain et al. (1998), who interpreted the apparently lower emissivity along the jet axis as Doppler de-beamed radiation from a spine with plasma flow velocities faster than those of the sheath. Similar arguments, based on radio observations of the kpc jet of the FR I radio galaxy 3C 264 and on the pc jet of the FR I radio galaxy M87, were presented by Lara et al. (2004) and Kovalev et al. (2007), respectively. A comprehensive multiwavelength study of the Kpc scale jet of M87 (Perlman et al. 2001; Perlman & Wilson 2005) shows stratification in the high-energy radiation production, in the sense that effective particle acceleration capable of producing the observed IR to X-ray synchrotron emission of M87 is concentrated along the spine of the jet. A recent study of the jets Centaurus A shows similar results, in the sense that the X-ray spectrum of the jet knots is harder along the spine (Worrall et al. 2008).

A model-independent argument for a spine-sheath geometry in the jet of PKS 0637-752, with the spine both (1) being faster and (2) emitting most of the IR to X-ray emission, can be constructed on the basis of multiwavelength observations and on the assumption that the quasar has two jets of similar power. This assumption is supported by the fact that in radio galaxies and quasars, the level of the presumably nonbeamed radio emission from the two lobes is comparable (e.g., Perley et al. 1997). The morphology of the western jet strongly suggests that the X-ray knots are part of the jet and not termination shocks. This is also supported by the fact that the western knot complex magnetic field orientation, determined by radio polarization measurements (Lovell et al. 2000), is parallel to the jet axis and not perpendicular, as one would expect from strong perpendicular shocks, typically found at the terminal hot spots. Radio observations (Lovell et al. 2000) show a radio feature diametrically opposite and at approximately the same distance from the core as the complex of the three knots WK 7.8, WK 8.9, and WK 9.7. Interestingly, the same parallel to the jet axis magnetic field orientation is observed at the eastern jet radio feature, suggesting that this is also not a terminal hotspot and that the jet plasma flows through the radio feature.

Assuming that the two jets are intrinsically symmetric, the ratio $j_r \approx 1.5$ of the jet to counterjet radio fluxes (see Figure 3 and Table 1) constrains the radio plasma speed $u_r = \beta_r c$ to be

$$\beta_r \cos\theta = \frac{j_r^{1/(3+a)} - 1}{j_r^{1/(3+a)} + 1} \approx 0.06, \tag{8}$$

where $a = 0.8$ is the radio spectral index and θ the jet orientation to the LOS. If the IR to X-ray emitting plasma had the same velocity as the radio, one would expect a clear detection of the counterjet in the IR to X-ray range. However, this is not the case and using the limit $j_X \gtrsim 100$ for the jet to counterjet X-ray ratio, one obtains $\beta_X \cos\theta \gtrsim 0.54$. The speed, therefore, of the X-ray emitting plasma must be significantly higher than that of the radio plasma. Similar, but somewhat lower, speed constraints can be derived using the IR and optical ratio limits.

5. CONCLUSIONS

We present new NICMOS and ACS observations, which we use, together with existing broadband observations, to build the most complete SED of the jet knots of quasar PKS 0637-752. We relax the equipartition assumption and show that in the EC/CMB framework for the X-ray emission, the plausible requirement that the 10″ jet is at most 1 Mpc long excludes magnetically-dominated jets. We also show that limits on the BC emission exclude e^-–e^+ jets in the EC/CMB framework, regardless of equipartition: the jet needs to carry some, or most of its power with protons. Interestingly, if we require one proton per radiation lepton, only the equipartition jet does not require substantially super-Eddington power. Taking radiative cooling into account, the Lorentz factor $\Gamma \sim 18$–20 required to model the knot SED for the equipartition solution is significantly higher than that used previously, and is more in agreement with the radio core limit $\Gamma > 17.4$, derived from core superluminal motions (Lovell et al. 2000). Configurations with significantly more than one proton per radiating lepton are excluded in the EC/CMB model. Finally, we note that the counterjet radio feature and its polarization, together with the limits on the IR-optical and X-ray emission, suggest a spine-sheath flow, with most of the IR-optical-X-ray emission coming from the spine.

Part of this work was done in the context of the senior thesis of Kushal Mehta at UMBC. The authors acknowledge support from LTSA grants # NAG5-9997 and NNG05GD63G at UMBC, as well as #NNX07AM17G at FIT, and from the *HST* observing grant GO-10541.01 at UMBC.

APPENDIX

THE PARAMETERS c_1, c_2

The parameters c_1 and c_2, using a δ-function approximation for the synchrotron and IC emissivity are given by

$$c_1 = \frac{4^{(p-2)/2}\sigma_\tau c U}{3^{(p-1)/2}} \left(\frac{h}{K_B T}\right)^{(3-p)/2},$$
$$c_2 = \frac{\sigma_\tau c B_{\rm crit}^{(3-p)/2}}{12\pi} \left(\frac{h}{m_e c^2}\right)^{(3-p)/2}, \tag{A1}$$

where $U$and T are the CMB photon energy density and temperature, respectively, at the redshift of the source, σ_τ is the Thomson cross section, and $B_{\rm crit} = \left(m_e^2 c^3\right)/(e\hbar)$ is the critical magnetic field.

REFERENCES

Arshakian, T. G., & Longair, M. S. 2004, MNRAS, 351, 727
Atoyan, A., & Dermer, C. D. 2004, ApJ, 613, 151
Blandford, R. D., & McKee, C. F. 1976, Phys. Fluids, 19, 1130
Celotti, A., Ghisellini, G., & Chiaberge, M. 2001, MNRAS, 321, L1
Chartas, G., et al. 2000, ApJ, 542, 655
Cheung, C. C., Stawarz, L., & Siemiginowska, A. 2006, ApJ, 650, 679
Dermer, C. D., & Atoyan, A. 2004, ApJ, 611, L9
Georganopoulos, M., & Kazanas, D. 2004, ApJ, 604, L81
Georganopoulos, M., Kazanas, D., Perlman, E. S., & McEnery, J. 2006, ApJ, 653, L5
Georganopoulos, M., Kazanas, D., Perlman, E. S., & Stecker, F. W. 2005, ApJ, 625, 656
Hardcastle, M. J., Harris, D. E., Worrall, D. M., & Birkinshaw, M. 2004, ApJ, 612, 729
Harris, D. E., & Krawczynski, H. 2006, ARA&A, 44, 463
Jester, S., Harris, D. E., Marshall, H. L., & Meisenheimer, K. 2006, ApJ, 648, 900
Jester, S., Meisenheimer, K., Martel, A. R., Perlman, E. S., & Sparks, W. B. 2007, MNRAS, 380, 828
Jorstad, S. G., & Marscher, A. P. 2004, ApJ, 614, 615
Kataoka, J., Edwards, P., Georganopoulos, M., Takahara, F., & Wagner, S. 2003, A&A, 399, 91
Kirk, J. G., Guthmann, A. W., Gallant, Y. A., & Achterberg, A. 2000, ApJ, 542, 235
Kovalev, Y. Y., Lister, M. L., Homan, D. C., & Kellermann, K. I. 2007, ApJ, 668, L27
Lara, L., Giovannini, G., Cotton, W. D., Feretti, L., & Venturi, T. 2004, A&A, 415, 905
Lovell, J. E. J., et al. 2000, in Astrophysical Phenomena Revealed by Space VLBI, ed. H. Hirabayashi, P. G. Edwards, & D. W. Murphy (Sagamihara: ISAS), 215
Marshall, H. L., et al. 2005, ApJS, 156, 13
Ostrowski, M. 2008, New Astron. Rev., in press, arXiv:0801.1339
Perley, R. A., Röser, H.-J., & Meisenheimer, K. 1997, A&A, 328, 12
Perlman, E. S., Biretta, J. A., Sparks, W. B., Macchetto, F. D., & Leahy, J. P. 2001, ApJ, 551, 206
Perlman, E. S., & Wilson, A. S. 2005, ApJ, 627, 140
Rieger, F. M., & Duffy, P. 2004, ApJ, 617, 155
Sambruna, R. M., Gambill, J. K., Maraschi, L., Tavecchio, F., Cerutti, R., Cheung, C. C., Urry, C. M., & Chartas, G. 2004, ApJ, 608, 698
Sambruna, R. M., Gliozzi, M., Donato, D., Maraschi, L., Tavecchio, F., Cheung, C. C., Urry, C. M., & Wardle, J. F. C. 2006, ApJ, 641, 717
Sambruna, R. M., Maraschi, L., Tavecchio, F., Urry, C. M., Cheung, C. C., Chartas, G., Scarpa, R., & Gambill, J. K. 2002, ApJ, 571, 206
Schwartz, D. A., et al. 2000, ApJ, 540, L69
Schwartz, D. A., et al. 2006, ApJ, 640, 592
Siemiginowska, A., Bechtold, J., Aldcroft, T. L., Elvis, M., Harris, D. E., & Dobrzycki, A. 2002, ApJ, 570, 543
Stawarz, Ł., & Ostrowski, M. 2002, ApJ, 578, 763
Swain, M. R., Bridle, A. H., & Baum, S. A. 1998, ApJ, 507, L29
Tavecchio, F., Maraschi, L., Sambruna, R. M., & Urry, C. M. 2000, ApJ, 544, L23
Uchiyama, Y., Urry, C. M., Van Duyne, J., Cheung, C. C., Sambruna, R. M., Takahashi, T., Tavecchio, F., & Maraschi, L. 2005, ApJ, 631, L113
Uchiyama, Y., et al. 2006, ApJ, 648, 910
Worrall, D. M., et al. 2008, ApJ, 673, L135